Inorganic Chemistry

pubs.acs.org/IC Article

Phosphorescence in Mn^{4+}-Doped R^{+}/R^{2+} Germanates (R^{+} = Na^{+} or K^{+}, R^{2+} = Sr^{2+})

Sergei A. Novikov, Yimin Lu, Weiguo Zhang, P. Shiv Halasyamani, Shruti Hariyani, Jakoah Brgoch, Vladislav V. Klepov, Hans-Conrad zur Loye, and Yurij Mozharivskyj*

Cite This: *Inorg. Chem.* 2022, 61, 9364−9374 Read Online

ABSTRACT: Single crystals of three new compounds, $Na_{0.36}Sr_{0.82}Ge_4O_9$ (**1**, proposed composition), $Na_2SrGe_6O_{14}$ (**2**), and $K_2SrGe_8O_{18}$ (**3**), were obtained and characterized using single-crystal X-ray diffraction. Their structures contain three-dimensional (3D) anionic frameworks built from GeO_4 and GeO_6 polyhedra. The presence of octahedral Ge^{4+} sites makes the new phases suitable for Mn^{4+} substitution to obtain red-emitting phosphors with a potential application for light conversion. Photoluminescence properties of Mn^{4+}-substituted $Na_2SrGe_6O_{14}$ (**2**) and $K_2SrGe_8O_{18}$ (**3**) samples were studied over a range of temperatures, and red light photoluminescence associated with the electronic transitions of tetravalent manganese was observed. The $Na_2SrGe_6O_{14}$ (**2**) phase was also substituted with Pr^{3+} on the mixed Na−Sr site similar to the previously studied $Na_2CaGe_6O_{14}$:Pr^{3+}. The red emission peak of the Pr^{3+} activator occurs at a shorter wavelength (610 nm) compared to that of Mn^{4+} (662−663 nm). Additionally, second harmonic generation (SHG) data were collected for the noncentrosymmetric $Na_2SrGe_6O_{14}$ (**2**) phase, indicating weak SHG activity. Diffuse reflectance spectroscopy and density of states calculations were performed to estimate the band gap values for pristine $Na_2SrGe_6O_{14}$ (**2**) and $K_2SrGe_8O_{18}$ (**3**) phases.

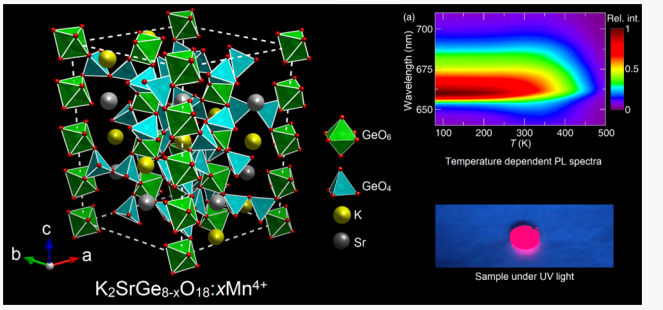

1. INTRODUCTION

New compounds featuring unique germanate frameworks in their structures exhibit important physical properties.[1−4] More specifically, germanates with simultaneous tetrahedral and octahedral coordination of Ge^{4+} are of interest both from the fundamental and practical aspects. These compounds can be used to mimic some high-pressure silicates, in which silicon atoms can adopt an octahedral coordination as well.[5] From the application perspective, the octahedrally coordinated Ge^{4+} sites are attractive due to their potential phosphorescence upon the transition metal substitution[6−13] and nonlinear optical[14] and piezoelectric properties.[15] In particular, the similar size[16] and oxidation state of Mn^{4+} and Ge^{4+} enable the substitution of the octahedral Ge^{4+} sites with Mn^{4+}, often yielding red-emitting phosphors,[7−11,17] which can be suitable for phosphor-converted light-emitting diode (LED) devices.[18−20] There are several advantages of Mn^{4+}, such as strong absorption in the ultraviolet (UV)−blue region, an intense emission band in the red region of the visible spectrum, and in the case of the oxides, relatively simple preparation.[7−11,17] The known drawbacks of Mn^{4+} phosphors are thermal and concentration quenching of luminescence.[9,13] The latter, however, can be employed for thermal sensing applications.[21−23]

Substituting in the germanate phases is not limited to Mn^{4+} since the larger cationic sites can accommodate lanthanides[24−26] or Bi^{3+}.[27] For example, langasite[28]-type $Na_2CaGe_6O_{14}$ shows thermal-sensitizing phosphorescence when doped with Pr^{3+}.[24] Noncentrosymmetric $Na_2CaGe_6O_{14}$, which crystallizes with the *P*321 space group, is also interesting due to its piezoelectric properties.[15] Nonlinear optical properties of the related phase, $Na_2SrGe_6O_{14}$, were also investigated[14] but no structural data have been deposited in the inorganic crystal structure database (ICSD).[29]

Among germanate-based Mn^{4+} phosphors, tetragermanates containing alkali ($R_2Ge_4O_9$, *R* = Li−Rb) and the alkaline-earth (RGe_4O_9, *R* = Sr, Ba) metals are well studied both structurally[30−34] and optically.[6−9,11,13] The anionic frameworks of these tetragermanates are built from GeO_4 and GeO_6 polyhedra. Despite the same stoichiometry of these anionic frameworks, the structures of $R_nGe_4O_9$ (n = 1 or 2) compounds are different. For example, the compounds in the Na−Rb series are trigonal and centrosymmetric ($P\bar{3}c1$ space group), whereas Sr and Ba phases are noncentrosymmetric

Received: April 21, 2022
Published: June 8, 2022

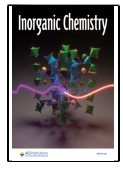

https://doi.org/10.1021/acs.inorgchem.2c01364
Inorg. Chem. 2022, 61, 9364−9374

Table 1. Selected Crystallographic Data and Refinement Results for 1−3

compound	1	2	3
formula	$Na_{0.36}Sr_{0.82}Ge_4O_9$[a]	$Na_2SrGe_6O_{14}$	$K_2SrGe_8O_{18}$
formula weight	514.47	793.12	1034.54
crystal system	trigonal		
space group	*R*32	*P*321	$P\bar{3}c1$
a (Å)	11.3584(13)	8.2322(12)	11.5937(16)
c (Å)	4.6701(15)	4.8677(10)	19.225(4)
flack parameter	0.01(2)	−0.054(19)	
volume (Å^3)	521.8(2)	285.68(8)	2237.9(6)
Z	3	1	6
ρ_{calcg} (cm^3)	4.946	4.610	4.606
μ (mm^{-1})	24.730	20.361	20.088
F(000)	705	364	2856
2Θ range (°)	7.18−69.64	5.72−69.66	5.87−69.88
index ranges	$-14 \le h \le 15$, $-18 \le k \le 18$, $-7 \le l \le 3$	$-13 \le h \le 13$, $-13 \le k \le 13$, $-7 \le l \le 7$	$-18 \le h \le 18$, $-18 \le k \le 13$, $-30 \le l \le 30$
reflections collected	1922	5196	25219
data/restraints/parameters	507/0/30	846/0/38	3273/0/134
GOOF	1.073	1.203	1.044
R_1 (I > 2σ (I))	0.0160	0.0194	0.0653
largest diff. peak/hole (e/Å^3)	0.54/−0.96	0.88/−0.68	3.01/−2.40

[a]Electron density from the experiment was ≈5.86 e$^-$(or 0.154 of the Sr atom). If x is the Na occupancy and y is the Sr occupancy, then $11x + 38y = 5.86$. The total charge from Na and Sr is +2 to balance $Ge_4O_9^{2-}$. Considering the symmetry of the structure, the total charge on the mixed Na^+/Sr^{2+} site should be +1/3. Thus, $x + 2y = 1/3$. From these two equations, x and y were found to be ≈0.060 and ≈0.137, respectively, giving the $Na_{0.36}Sr_{0.82}Ge_4O_9$ formula.

(*P*321 space group). In contrast, the Li phase exhibits a lower symmetry, crystallizing with the acentric orthorhombic space group $P2_1$ *ca*.[34] Such variations are associated with different radii and charges of R^+ and R^{2+} cations. Interestingly, $Na_2Ge_4O_9$ forms a metastable phase, while the lack of the reliable structural data on *R* = Mg and Ca tetragermantates may indicate their lower thermodynamic stability as compared to the other phases.[32]

In this report, we describe the synthesis, structure, and optical properties of three new compounds based on germanate frameworks: tetragermanate $Na_{0.36}Sr_{0.82}Ge_4O_9$ (**1**), langasite-type $Na_2SrGe_6O_{14}$ (**2**), and octagermanate $K_2SrGe_8O_{18}$ (**3**), isostructural to $K_2BaGe_8O_{18}$.[35] The new phases were successfully doped with Mn^{4+} (phases **2** and **3**) and Pr^{3+} (phase **2**) to explore their photoluminescence properties. As $Na_2SrGe_6O_{14}$ (**2**) crystallizes in a non-centrosymmetric space group, its second harmonic generation (SHG) response was measured.

2. EXPERIMENTAL SECTION

Powders of GeO_2 (99.999 wt %), $KHCO_3$ (99 wt %), NaCl (99 wt %), Na_2CO_3 (99.5 wt %), $SrCl_2$ (99 wt %), $SrCO_3$ (99 wt %) $MnCO_3$ (99.9 wt %), $Mn(CH_3COO)_2{\cdot}4H_2O$ (99.999 wt %), and Pr_6O_{11} (99.9 wt %) were used as received.

2.1. Synthesis of the New Phases as Single Crystals. The reagents in the calculated ratios were thoroughly ground in an agate mortar and pressed into pellets. The pellets were placed into a platinum crucible and thermally treated as described below. Note that the use of alumina or silica reaction vessels results in Al or Si admixtures on the Ge sites; thus, the use of platinum crucibles in these reactions was essential to obtain pure Ge phases.

$Na_{0.36}Sr_{0.82}Ge_4O_9$ (**1**) crystals were obtained while targeting $Na_{2x}Sr_{1-x}Ge_4O_9$ phases. When carbonate precursors were used during the synthesis instead of chloride precursors, $Na_2SrGe_6O_{14}$ (**2**) crystals were obtained. The attempts to obtain the hypothetical $K_2SrGe_6O_{14}$ phase yielded the octagermanate phase, $K_2SrGe_8O_{18}$ (**3**). The synthetic conditions and molar ratios shown below yielded single crystals of the new phases suitable for single-crystal X-ray diffraction (yet not the target phases).

$Na_{0.36}Sr_{0.82}Ge_4O_9$ (**1**) crystals were obtained in a reaction between NaCl (0.0094 g), $SrCl_2$ (0.0383 g), and GeO_2 (0.1348 g) in a 0.50:0.75:4.0 molar ratio. A pellet of the starting materials was heated to 1050 °C at a rate of 200 °C/h and dwelled at this temperature for 18 h, after which the furnace was cooled to 700 °C at a rate of 6 °C/h and switched off.

Single crystals of $Na_2SrGe_6O_{14}$ (**2**) were obtained by reacting Na_2CO_3 (0.0492 g) with $SrCO_3$ (0.0086 g) and GeO_2 (0.1214 g) in a 1.6:0.20:4.0 molar ratio. The sample pellet was heated to 1050 °C at a rate of 200 °C/h and dwelled for 2 h at this temperature. The reaction was cooled to 900 °C at a rate of 100 °C/h and then to 800 °C at 10 °C/h rate. Further cooling to room temperature was done by switching off the furnace.

Single crystals of $K_2SrGe_8O_{18}$ (**3**) were obtained in a reaction between $KHCO_3$ (0.0392 g), $SrCO_3$ (0.0289 g), and GeO_2 (0.1228 g) in a 2:1:6 molar ratio. The sample pellet was heated to 1050 °C at a rate of 200 °C/h. After 2 h, the furnace was cooled down to 950 °C at a rate of 50 °C/h and then to 850 °C at 10 °C/h rate. Further cooling to room temperature was done by switching off the furnace.

2.2. Single-Crystal X-ray Diffraction. The single crystals of **1**−**3** that were suitable for X-ray diffraction (XRD) were picked manually. The experimental data for **1**−**3** were collected at room temperature on an STOE IPDS II diffractometer (Mo Kα radiation) equipped with an image-plate type detector. The numerical absorption correction was performed by optimizing the crystal shape against equivalent reflections with X-Shape software.[36] The initial structure solution was done with SHELXT[37] software and refined using SHELXL software by full-matrix least-squares refinements.[38] The solution and refinement programs were run via the OLEX2 interface.[39] The crystallographic data and refinement results are summarized in Table 1. Compositions of the single crystals were determined based on the single-crystal diffraction. In $Na_{0.36}Sr_{0.82}Ge_4O_9$ (**1**), the composition of the mixed Na/Sr site was determined based on the two constraints: (1) the density of the Na/Sr site equals the refined electron density and (2) the charge of the

https://doi.org/10.1021/acs.inorgchem.2c01364
Inorg. Chem. 2022, 61, 9364−9374

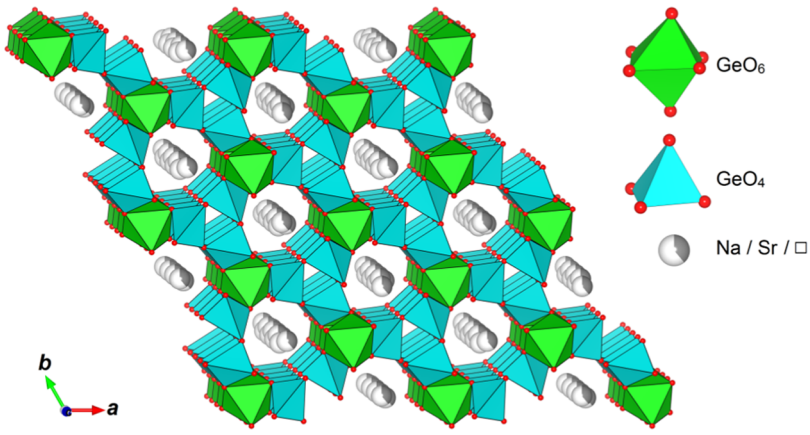

Figure 1. View of the $Na_{0.36}Sr_{0.82}Ge_4O_9$ (**1**) structure fragment along the *c* direction. Hereinafter, GeO_6 octahedra are green, GeO_4 tetrahedra are cyan, and oxygen atoms are red. Na^+ and Sr^{2+} cations are gray (with □ representing the deficiency).

Na/Sr site balances the charge of the $Ge_4O_9^{2-}$ framework (more details are in the footnote of Table 1).

2.3. Synthesis of the New Germanate Phosphors by the Solid-State Reaction. $Na_2SrGe_{6-x}O_{14}$:$x$$Mn^{4+}$ (**2**) samples were prepared through a solid-state reaction between Na_2CO_3, $SrCO_3$, GeO_2, and $MnCO_3$ in a 2:1:(6−x):x ratio, where x = 0.002, 0.008, and 0.016. The reagents were ground, pressed into a pellet, and annealed at 950 °C for 12 h. The $Na_2Sr_{1-x}Ge_6O_{14}$:$x$$Pr^{3+}$ sample was prepared in a similar way with a molar ratio of 2:0.994:6:0.001 for Na_2CO_3, $SrCO_3$, GeO_2, and Pr_6O_{11}, respectively. Note that a 4:1 Na:Sr molar ratio was initially proposed for the solid-state synthesis of $Na_2SrGe_6O_{14}$ (i.e., two times Na excess based on the stoichiometry) because the exact 1:1 ratio resulted in the formation of the significant amount of the $SrGe_4O_9$ phase. We found, however, that the purest $Na_2SrGe_6O_{14}$ product can be obtained with a slight excess of sodium ($Na_2CO_3/SrCO_3$ = 1.2:1).

Samples of $K_2SrGe_{8-x}O_{18}$:$x$$Mn^{4+}$ were synthesized by solid-state reactions between $SrCO_3$, $KHCO_3$, GeO_2, $MnCO_3$, or $Mn(CH_3COO)_2{\cdot}4H_2O$ in a 2:1:(8−x):x ratio, where x = 0.003, 0.005, 0.016, and 0.032. The mixtures were ground, pressed into a pellet, and annealed at 950 °C for 8 h. Second annealing for another 8 h at 950 °C was done for each sample after regrinding and pressing it into a pellet. To avoid the formation of side products, such as $SrGe_4O_9$, a very thorough grinding is required before each annealing. Alternatively, the $K_2SrGe_8O_{18}$ phase can be prepared by the solid-state reaction between $K_2Ge_4O_9$ and $SrGe_4O_9$ in a 1:1 molar ratio. This route is much slower and takes 3 to 4 annealing steps for every 24 h.

The powder X-ray diffraction data of $Na_2SrGe_6O_{14}$ (**2**) and $K_2SrGe_8O_{18}$ (**3**) prepared via the solid-state route were collected on a PANalytical X'Pert PRO diffractometer equipped with a germanium monochromator (Cu Kα_1 radiation) in the 20−80° 2θ range. The Rietveld refinement[40] results are provided in the Supporting Information (Figures S1 and S2).

2.4. Photoluminescence Measurements. Absorption and emission spectra of the prepared $Na_2SrGe_6O_{14}$ (**2**)- and $K_2SrGe_8O_{18}$ (**3**)-based phosphors were collected on an Agilent Cary Eclipse fluorescence spectrophotometer at room temperature.

For the temperature-dependent photoluminescence measurements, polycrystalline samples of $Na_2SrGe_6O_{14}$:Mn^{4+} and $K_2SrGe_8O_{18}$:Mn^{4+} were combined with an optically transparent resin (United Adhesives) and deposited onto a quartz slide (Chemglass). Temperature-dependent emission spectra from 80 to 500 K were obtained using a Janis cryostat (VPF-100) and a PTI fluorescence spectrophotometer with a 75 W xenon arc lamp for excitation.

2.5. Second Harmonic Generation (SHG) Measurements. SHG measurements were performed on powders using a pulsed neodymium-doped yttrium aluminum garnet (Nd:YAG) laser (Quantel Ultra 50) with a wavelength of 1064 nm. Ground crystalline α-SiO_2 was used as a reference SHG material. For $Na_2SrGe_6O_{14}$, the SHG intensity is roughly 0.9 of α-SiO_2. The sample was slightly impure. The impurity phase was $SrGe_4O_9$ (<1 wt %), which is also noncentrosymmetric. A pure sample of $SrGe_4O_9$ was obtained, and its activity was measured for comparison. The SHG activity of the $SrGe_4O_9$ phase was found to be much lower than that of $Na_2SrGe_6O_{14}$ (0.4 of α-SiO_2) and thus should not significantly impact the $Na_2SrGe_6O_{14}$ SHG measurement.

2.6. Band Gap Calculations and Experimental Measurement. UV−visible reflectance data were collected on a Varian Cary 5000 scan UV−vis−near-infrared (NIR) spectrophotometer over the 200−2000 nm spectral range at room temperature. Poly(tetrafluoroethylene) was used as a reference material. The reflectance spectrum was converted to absorbance using the Kubelka−Munk function.[41,42]

First principles calculations were performed using density functional theory (DFT) with a Vienna Ab initio Simulation Package (VASP) plane-wave code,[43,44] generalized gradient approximation of Perdew, Burke, and Ernzerhof (PBE),[45] and projector augmented wave (PAW) method.[46,47] The Na, K, Sr, Ge, and O valence electron configurations considered for the construction of PAW potentials were $2p^63s^1$, $3s^23p^64s^1$, $4s^24p^65s^2$, $4s^23d^{10}4p^2$, and $2s^22p^4$, respectively. To eliminate partial occupancy on the Sr/Na site in $Na_2SrGe_6O_{14}$, the symmetry of the structure was lowered to triclinic and 2 of 3 equiv sites were assigned to Na. Spin-polarized calculations were performed with 520 eV cutoff energy for the plane-wave basis set, 10^{-6} eV energy convergence criteria, and 5 × 5 × 7 and 3 × 3 × 2 *k*-point meshes for $Na_2SrGe_6O_{14}$ and $K_2SrGe_8O_{18}$. The ground-state geometries at 0 K were optimized by relaxing the cell volume, atomic positions, and cell symmetry until the maximum force on each atom is less than 0.001 eV/Å.

3. RESULTS AND DISCUSSION

3.1. Crystal Structure. *3.1.1. Phase (1): $Na_{0.36}Sr_{0.82}Ge_4O_9$ or γ-$SrGe_4O_9$.* The structure solution and refinement of $Na_{0.36}Sr_{0.82}Ge_4O_9$ were performed with the *R*32 space group. As we mentioned above, the electron density on the 9*e* Wyckoff position where the cations reside would be insufficient for a fully occupied Sr position. Additionally, the fully occupied Sr position would lead to a structure that is not charge balanced. Thus, the mixed Na−Sr site was accepted as a possible reason for the presence of the electron-density-deficient position.

There are two crystallographic Ge sites in the structure of this rhombohedral tetragermanate, octahedral Ge1 (3*b* Wyckoff position), and tetrahedrally coordinated Ge2 (9*d*). The Ge−O bond lengths are 1.891(3) Å for the six symmetrically equivalent Ge1−O bonds and 1.738(3)−1.758(2) Å for the Ge2−O bonds, which are in good agreement with the

https://doi.org/10.1021/acs.inorgchem.2c01364
Inorg. Chem. 2022, 61, 9364−9374

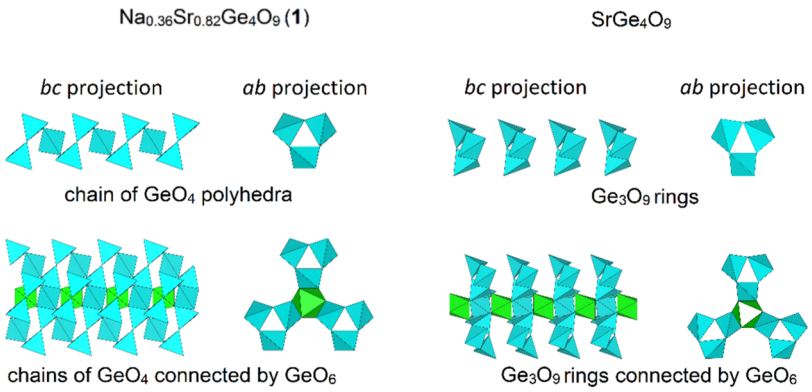

Figure 2. Comparison between GeO_n (n = 4 and 6) polyhedra connectivity in $Na_{0.36}Sr_{0.82}Ge_4O_9$ (**1**) and $SrGe_4O_9$.[31,31] Oxygen atoms are omitted.

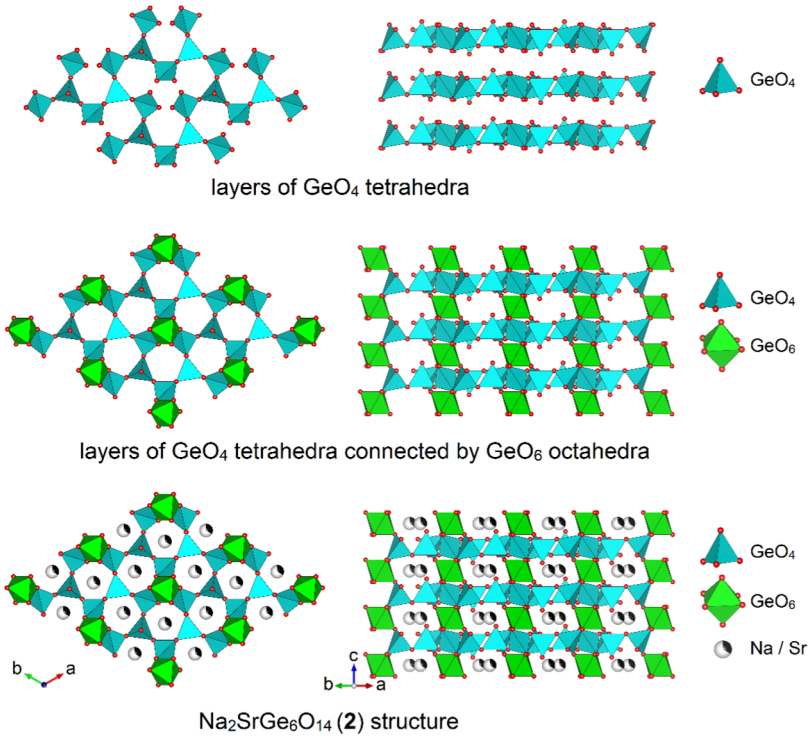

Figure 3. GeO_n polyhedra connectivity in $Na_2SrGe_6O_{14}$ (**2**) and a fragment of the $Na_2SrGe_6O_{14}$ (**2**) structure in two projections.

previously reported values.[48] The corner-sharing GeO_4 tetrahedra form infinite helical chains running along the c direction (Figure 1). These chains are linked into an infinite framework by the GeO_6 octahedra. Na and Sr cations share the same 9e site and occupy the channels within the anionic germanate framework.

In comparison to the previously reported tetragermanates, $SrGe_4O_9$[31] and $Na_2Ge_4O_9$,[32] the $Na_{0.36}Sr_{0.82}Ge_4O_9$ (**1**) structure containing mixed Na−Sr positions demonstrates new features. First, $Na_{0.36}Sr_{0.82}Ge_4O_9$ crystallizes with a rhombohedral unit cell, while the pure Na and pure Sr phases crystallize with primitive trigonal ones. Another feature of $Na_{0.36}Sr_{0.82}Ge_4O_9$ (**1**) is the cationic deficiency on the Na/Sr site, which is only 39% occupied by the cations. Thus, the chemical formula for **1** can also be written as $Na_{0.36}Sr_{0.82}\square_{1.82}Ge_4O_9$, with □ representing the deficiency.

When compared to $SrGe_4O_9$,[18] $Na_{0.36}Sr_{0.82}Ge_4O_9$ (**1**) has nearly the same unit cell dimensions but there is a significant topological difference between the two structures. As illustrated in Figure 2, the GeO_4 tetrahedra in $SrGe_4O_9$ form isolated rings that are stacked along the c direction and connected to each other through GeO_6 octahedra. In $Na_{0.36}Sr_{0.82}Ge_4O_9$ (**1**), the rings open, and two terminal GeO_4 units shift along the stacking direction, connecting to the adjacent units to form infinite helical chains (Figure 2). These chains and rings are further connected by GeO_6 octahedra. The topological analysis of the GeO_n polyhedra connectivity in **1** performed with ToposPro[49] software did not reveal any matches within the topological database. On the contrary, the germanate framework in $SrGe_4O_9$[31] resembles the titanate−silicate one in the naturally occurring $BaTiSi_3O_9$ compound[50] (a rare mineral benitoite). Thus, the cationic vacancies and the rare connectivity type of the germanate framework in the $Na_{0.36}Sr_{0.82}Ge_4O_9$ (**1**) phase establish that the phase formation cannot be described as a simple Na/Sr admixture in the $SrGe_4O_9$ structure.[31]

An alternative structure solution for phase **1** should be mentioned. The literature reports the γ-$PbGe_4O_9$ phase, a lead

https://doi.org/10.1021/acs.inorgchem.2c01364
Inorg. Chem. 2022, 61, 9364−9374

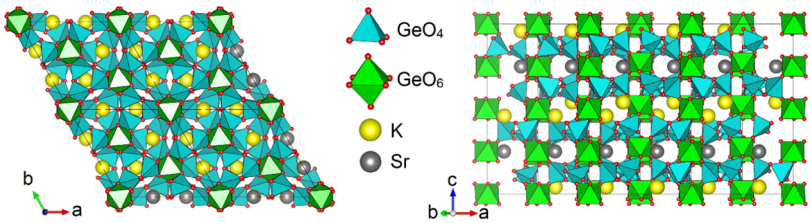

Figure 4. Fragment of the $K_2SrGe_8O_{18}$ (**3**) structure in two projections. K atoms are yellow and Sr atoms are gray.

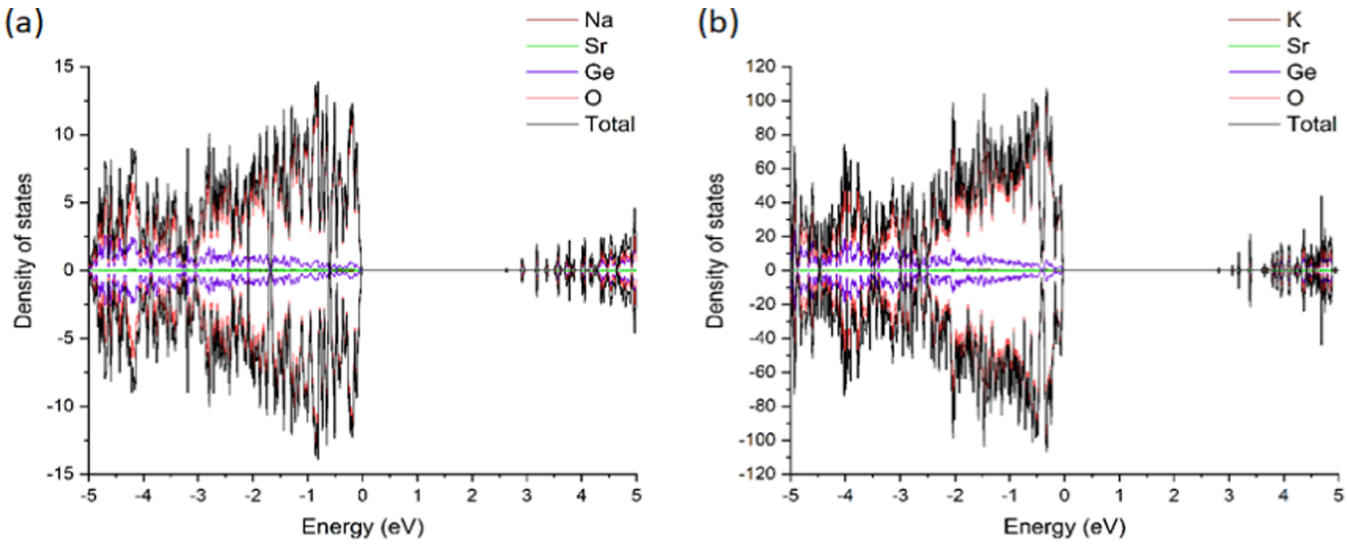

Figure 5. Density of states of $Na_2SrGe_6O_{14}$ (a) and $K_2SrGe_8O_{18}$ (b).

tetragermanate polymorph with the C_2 symmetry possessing a trigonal pseudosymmetry.[51] The structural similarities between phase **1** and γ-$PbGe_4O_9$ include the formation of the infinite helical chains from GeO_4 units. Because of these similarities, phase **1** can be considered as γ-$SrGe_4O_9$, since the structure solution and refinement can be done in the *C*2 space group as well, with a = 7.2490(14) Å, b = 11.333(2) Å, c = 4.6562(9) Å, and β = 115.45(3)°. However, the available experimental data casts doubt on the existence of the monoclinic γ-$SrGe_4O_9$. First, polymorphism of $SrGe_4O_9$ has never been reported as there is only one entry in ICSD for $SrGe_4O_9$, and it is for the trigonal *P*321 phase. Moreover, differential thermal analysis for $SrGe_4O_9$ shows no phase transition until the melting point (Figure S3). Second, there was no experimental evidence of twinning from our single-crystal XRD experiment (the data processed with Apex4[52]). Third, phase **1** was obtained in the presence of NaCl, which gives the possibility of mixed Sr/Na sites. If the synthesis is repeated under the same conditions, but in the absence of NaCl, the well-known trigonal $SrGe_4O_9$ phase forms. Finally, the Le Bail simulated diffraction pattern of the *R*32 cell demonstrates the same features as the experimental diffractogram (Figures S4 and S5). These features are not described in the *C*2 Le Bail simulation. Taking these points into account, we consider phase **1** as $Na_{0.36}Sr_{0.82}Ge_4O_9$.

*3.1.2. $Na_2SrGe_6O_{14}$ (**2**).* The Ge atoms in $Na_2SrGe_6O_{14}$ occupy three sites: 3*f* (Ge1), 1*a* (Ge2), and 2*d* (Ge3). Ge2 is octahedrally coordinated by oxygen, while Ge1 and Ge3 adopt a tetrahedral environment. GeO_4 tetrahedra share corners to form infinite layers that are parallel to the *ab* plane (Figure 3 top). The neighboring layers are connected into a 3D anionic framework by the GeO_6 polyhedra (Figure 3 center). The channels of this framework are occupied by Na and Sr cations (Figure 3 bottom). The Na and Sr cations share the 3*e* site in a 2:1 ratio, giving the $Na_2SrGe_6O_{14}$ composition.

The $Na_2SrGe_6O_{14}$ (**2**) structure demonstrates the same features as $Na_2CaGe_6O_{14}$ one.[15] Ge2 is surrounded by six oxygen atoms forming a regular octahedron. $Ge1O_4$ is slightly distorted (with two shorter and two longer Ge−O bonds), while the distortion of the Ge3 tetrahedral surrounding is more pronounced. One of the Ge−O bonds (1.68 Å) is much shorter than the three other (1.76 Å). Overall, the $Na_2SrGe_6O_{14}$ (**2**) phase adopts a langasite-type[53] crystal structure.

*3.1.3. $K_2SrGe_8O_{18}$ (**3**).* Similar to **1** and **2**, the $K_2SrGe_8O_{18}$ (**3**) structure contains germanium atoms in both octahedral and tetrahedral oxygen environments. Three tetrahedrally coordinated Ge atoms occupy general positions, while four octahedrally coordinated ones are located in special positions. In contrast to **1** and **2**, K and Sr atoms occupy two distinct crystallographic sites in **3**, 12*g* (K) and 6*f* (Sr). As in **1** and **2**, GeO_4 and GeO_6 polyhedra are connected to form an anionic framework. The arrangement of the Ge polyhedra in **3** is similar to that in $K_2Ge_4O_9$[33] and $SrGe_4O_9$[31] with 0D Ge_3O_9 rings connected by GeO_6 octahedra through corner sharing (Figure 4).

$K_2SrGe_8O_{18}$ (**3**) and $K_2Ge_4O_9$[33] crystallize with the $P\bar{3}c1$ space group, while $SrGe_4O_9$ adopts the noncentrosymmetric *P*321 group.[31] Despite the similar stoichiometries and germanium polyhedra arrangements, there is a subtle difference between these three structures resulting from differences in the GeO_n polyhedra connectivity. This connectivity difference for some germanate structures has been analyzed

https://doi.org/10.1021/acs.inorgchem.2c01364
Inorg. Chem. 2022, 61, 9364−9374

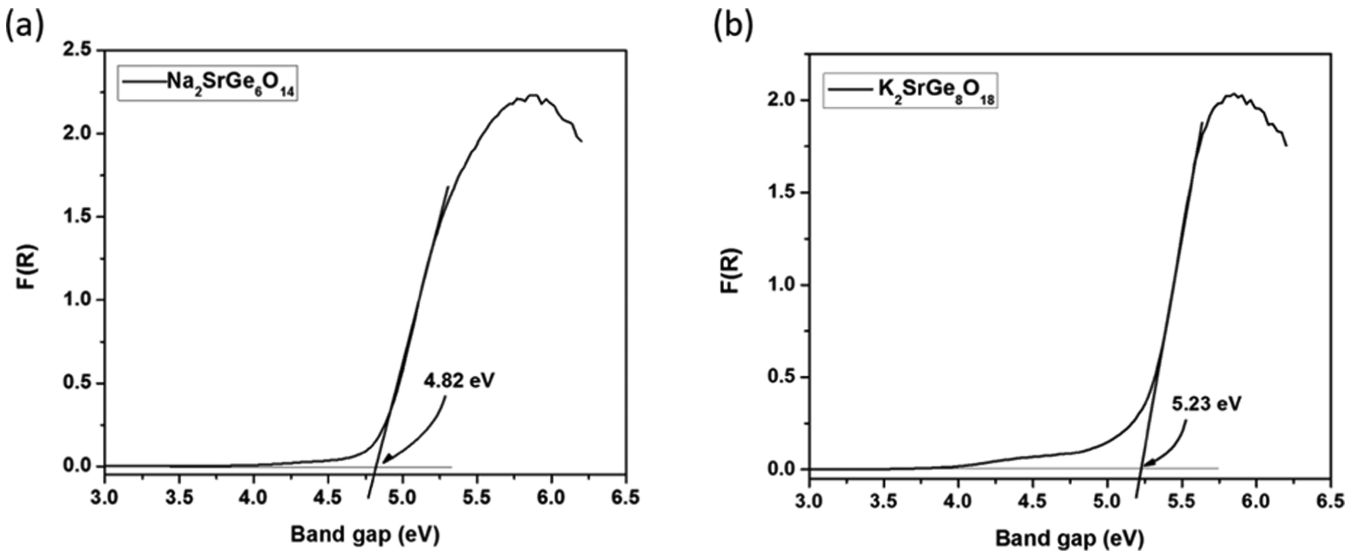

Figure 6. F(R) vs energy (in eV) plot for the pristine $Na_2SrGe_6O_{14}$ (a) and $K_2SrGe_8O_{18}$ (b) phases. The corresponding optical band gap values are given on the plot.

in a previous work on $Na_2BaGe_8O_{18}$ and $Rb_2BaGe_8O_{18}$ phases.[54]

3.2. Calculated and Experimental Band Gap. The electronic structures of $Na_2SrGe_6O_{14}$ and $K_2SrGe_8O_{18}$ were calculated using ab initio methods (Figure 5). In both compounds, the top of the valence band consists mostly of O states, whereas the bottom of the conduction band consists of both Ge states with a significant contribution from the O orbitals. The theoretical band gaps, 2.61 and 2.78 eV for $Na_2SrGe_6O_{14}$ and $K_2SrGe_8O_{18}$, respectively, indicate insulating behavior in both oxides.

The calculated values of the band gaps for **2** and **3** are significantly lower than the experimental data (Figure 6): 2.61 and 2.78 eV vs 4.82 and 5.23 eV for $Na_2SrGe_6O_{14}$ and $K_2SrGe_8O_{18}$, respectively. The mismatch is the result of the known drawbacks of DFT calculations of insulators using the PBE functional. The magnitude of the mismatch for our calculations is comparable to that of another germanate phosphor material, $Li_3RbGe_8O_{18}$, where the calculated band gap is 2.72 eV, while the experimental one is measured to be 5.26 eV.[10]

3.3. Photoluminescence Properties of the Pr^{3+} and Mn^{4+} Activated Germanates. A phosphor was prepared from the $Na_2SrGe_6O_{14}$ phase via Pr^{3+} doping, and the photoluminescence (PL) emission and excitation (PLE) spectra were collected (Figure 7). The Pr^{3+} content was 0.6 mol %, which is identical to that of the previously studied $Na_2CaGe_6O_{14}$.[24] Under the UV excitation ($\lambda_{ex.}$ = 246 nm), the $Na_2Sr_{0.994}Ge_6O_{14}$:0.006 Pr^{3+} sample demonstrates the same emission features as Pr^{3+}-substituted $Na_2CaGe_6O_{14}$:[24] one emission peak at 493 ($^3P_0 \rightarrow {}^3H_4$ transition) and a second, dominating emission peak at 610 nm ($^1D_2 \rightarrow {}^3H_4$ transition) in the visible region (Figure 7). The peaks are slightly shifted (1−2 nm) compared to $Na_2CaGe_6O_{14}$, where the corresponding peaks occur at 492 and 612 nm.[24]

The octahedral Ge site in the $Na_2SrGe_6O_{14}$ (**2**) structure was doped with Mn^{4+}, and the PL and PLE spectra were collected (Figure 8a) for the corresponding samples. This material has two distinct absorption maxima. The first and dominant absorption peak is located in the UV region at 290 nm, and the second is in the visible region ≈440 nm. The latter

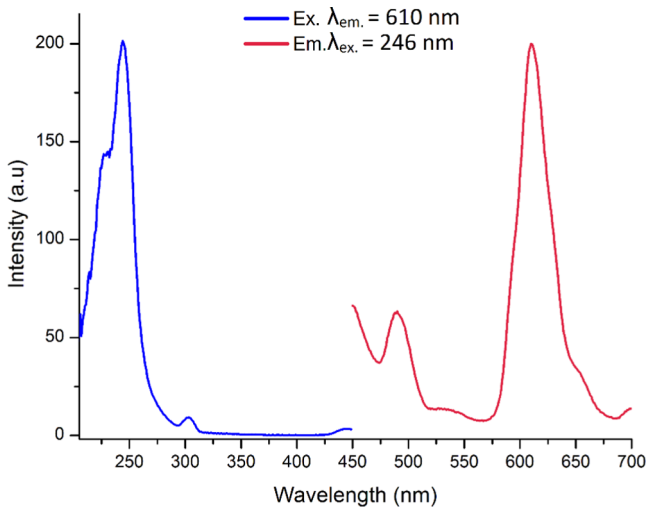

Figure 7. PLE and PL spectra of the $Na_2Sr_{0.994}Ge_6O_{14}$:0.006 Pr^{3+} sample at room temperature.

is associated with the $^4T_{2g} \leftarrow {}^4A_{2g}$ transition of the Mn^{4+} ion. The UV absorption band is asymmetric and likely formed by the overlap of the O^{2-} to Mn^{4+} charge-transfer band and the allowed $^4T_{1g} \leftarrow {}^4A_{2g}$ electron transitions of Mn^{4+}.[55]

The emission peak at 663 nm is associated with $^2E_g \rightarrow {}^4A_{2g}$ relaxation of Mn^{4+} and the peak position is in good agreement with previous reports of Mn^{4+} phosphors.[56−60] The position of the emission peak is known to be independent on the crystal field strength but affected by the covalency of Mn−ligand bonds.[61]

The performance of the $Na_2SrGe_{6-x}O_{14}$:xMn^{4+} (x = 0.002, 0.008, 0.016) phosphor was optimized by adjusting the activator substitution level. We found that the $Na_2SrGe_{5.992}O_{14}$:0.008Mn^{4+} sample exhibits a much higher emission intensity compared with the initially prepared $Na_2SrGe_{5.998}O_{14}$:0.002Mn^{4+} sample (Figure 8b), whereas a higher substitution level of Mn^{4+} leads to luminescence quenching and a decrease in the emission intensity.

The PLE and PL data for the Mn^{4+}-doped $K_2SrGe_8O_{18}$ (**3**) samples were collected at room temperature (Figure 9a). The

https://doi.org/10.1021/acs.inorgchem.2c01364
Inorg. Chem. 2022, 61, 9364−9374

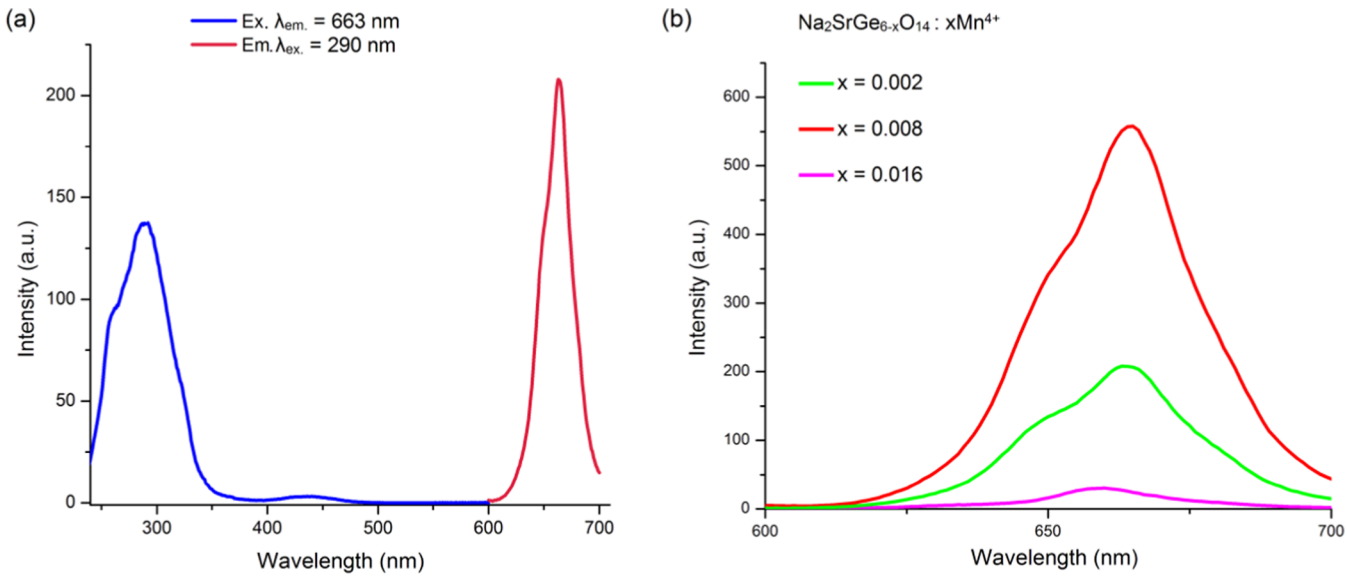

Figure 8. PLE and PL spectra of the $Na_2SrGe_{5.998}O_{14}$:0.002Mn^{4+} sample (a) and the PL emission spectra of the $Na_2SrGe_{6-x}O_{14}$:$x$$Mn^{4+}$ series (x = 0.002, 0.008, and 0.016) (b).

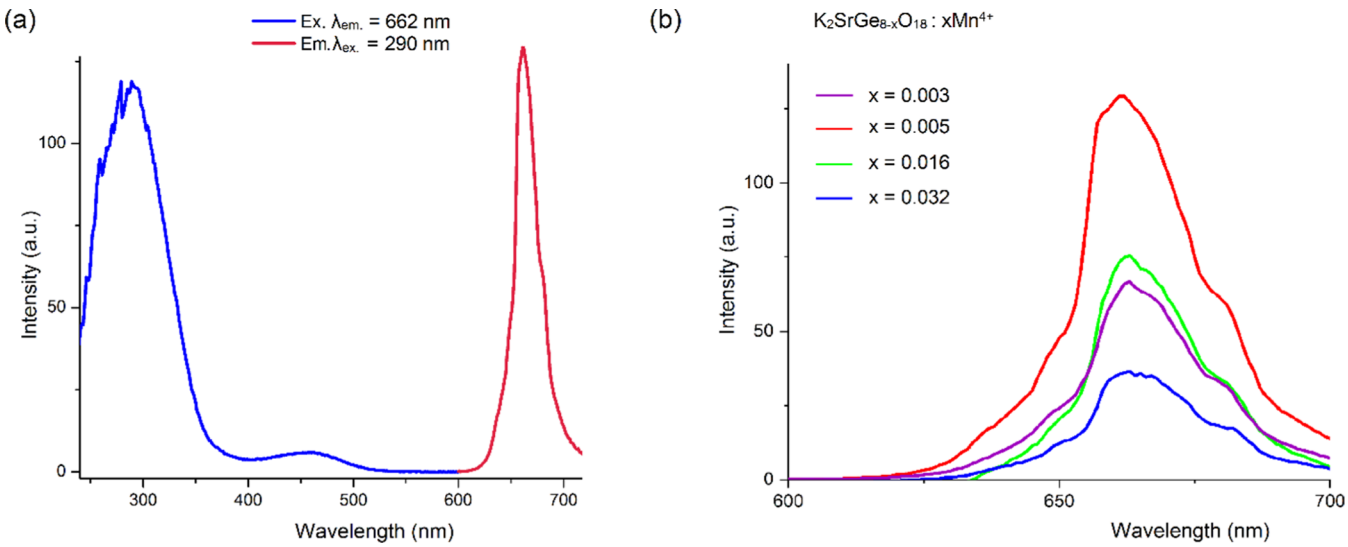

Figure 9. PLE and PL spectra of the $K_2SrGe_{7.995}O_{18}$:0.005Mn^{4+} sample (a) and the PL emission spectra of $K_2SrGe_{8-x}O_{18}$:$x$$Mn^{4+}$ (x = 0.003, 0.005, 0.016, and 0.032) (b).

emission peak positions are close to those observed from $Na_2SrGe_6O_{14}$:Mn^{4+}. Under UV excitation, the sample emits red light with a narrow peak at 662 nm. This data is in good agreement with other reported Mn^{4+}-substituted germanate phases.[6,11,62] $K_2SrGe_{7.995}O_{18}$:0.005Mn^{4+} exhibits the highest emission intensity (Figure 9b) in the series.

For both $Na_2SrGe_6O_{14}$ (**2**) and $K_2SrGe_8O_{18}$ (**3**), the approximate positions of the $^4T_{1g} \leftarrow {}^4A_{2g}$ (^4F) peaks overlap with the charge-transfer peaks, which can be estimated from the following equations[63]

$$D_q = E(^4T_{2g} \leftarrow {}^4A_{2g})/10 \quad (1)$$

$$\frac{D_q}{B} = \frac{15(x-8)}{x^2 - 10x} \quad (2)$$

$$x = \frac{E(^4T_{1g} \leftarrow {}^4A_{2g}) - E(^4T_{2g} \leftarrow {}^4A_{2g})}{D_q} \quad (3)$$

$$\frac{E(^2E_g \rightarrow {}^4A_{2g})}{B} = \frac{3.05C}{B} + 7.9 - \frac{1.8B}{D_q} \quad (4)$$

where D_q is a crystal field strength for Mn^{4+} and B and C are Racah parameters.

If a free Mn^{4+} cation is introduced into a crystal field, the Racah parameters are reduced due to the nephelauxetic effect.[64] The magnitude of this effect depends on the covalency of the Mn−ligand bonds and influences the optical properties of Mn^{4+}-substituted phosphors. The nephelauxetic ratio β_1, suggested by Brik et al.,[61] has a linear correlation to the energy of the ^2E_g level (i.e., the emission frequency, cm^{-1})

$$E(^2E_g \rightarrow {}^4A_{2g}) = -880.49 + 16261.92\,\beta_1 \quad (5)$$

https://doi.org/10.1021/acs.inorgchem.2c01364
Inorg. Chem. 2022, 61, 9364−9374

where

$$\beta_1 = \sqrt{\left(\frac{B}{B_0}\right)^2 + \left(\frac{C}{C_0}\right)^2} \quad (6)$$

(B_0 = 1160 cm^{-1} and C_0 = 4303 cm^{-1} are free Mn^{4+} Racah parameters[65]). The results of the calculations for $Na_2SrGe_6O_{14}$ (**2**) and $K_2SrGe_8O_{18}$ (**3**) are summarized in Table 2. The calculated positions of the $^4T_{1g} \leftarrow {}^4A_{2g}$ absorption peaks are 328 and 337 nm for $Na_2SrGe_6O_{14}$ (**2**) and $K_2SrGe_8O_{18}$ (**3**), respectively.

Table 2. PLE and PL Parameters of the Mn^{4+}-Doped $Na_2SrGe_6O_{14}$ (2) and $K_2SrGe_8O_{18}$ (3) Samples[a]

sample	D_q (cm^{-1})	B (cm^{-1})	C (cm^{-1})	β_1	$E(^2E_g)$ (cm^{-1})	$E(^4T_{1g})$ (cm^{-1})
$Na_2SrGe_6O_{14}$ (**2**)	2252	774	3099	0.982	15 083	30 520
$K_2SrGe_8O_{18}$ (**3**)	2174	771	3117	0.983	15 106	29 664

[a]The values of B, C, and $E(^4T_{1g})$ are calculated from eqs 1−6 and may vary from the experimental data.

The calculated values of the crystal field parameters D_q, B, and C, and the nephelauxetic ratio β_1 for **2** and **3** are close to those reported for the $K_2Ge_4O_9$ phase at room temperature.[66] The Mn^{4+} cation in the oxide matrix with the more covalent bonds typically has $\beta_1 < 1$, while in the fluoride matrix with more ionic bonds, this value exceeds 1.[61] Thus, the β_1 values for $Na_2SrGe_6O_{14}$ (**2**) and $K_2SrGe_8O_{18}$ (**3**) are in the typical covalent oxide region.

3.4. Temperature-Dependent Phosphorescence in $Na_2SrGe_6O_{14}$ (2) and $K_2SrGe_8O_{18}$ (3). Photoluminescence thermal quenching is one of the limitations of transition-metal-based luminescent materials. To study the change in the emission intensity as a function of temperature, temperature-dependent luminescence spectra were collected for the $Na_2SrGe_{5.992}O_{14}$:0.008Mn^{4+} and $K_2SrGe_{7.995}O_{18}$:0.005Mn^{4+} samples (Figures S6 and S7 in the Supporting Information). The emission from the $Na_2SrGe_{5.992}O_{14}$:0.008Mn^{4+} sample was weak and demonstrated significant artifacts; for that reason, only the data for $K_2SrGe_{7.995}O_{18}$:0.005Mn^{4+} are shown below.

Figure 10 includes a contour plot of the temperature-dependent PL spectra for the $K_2SrGe_{7.995}O_{18}$:0.005Mn^{4+} sample (Figure 10a) and the normalized integrated intensity data for the 77−500 K temperature range (Figure 10b). As expected, the increasing temperature results in the decrease in the photoluminescence intensity, which gradually drops to 50% of the low-temperature emission intensity at 420 K (Figure 10b). The decrease in the photoluminescence intensity at the elevated temperatures originates from the higher probability of the nonradiative relaxation.[55] It can be illustrated with a configurational coordinate diagram: at elevated temperatures, the relaxation from the ^2E_g state may occur to the $^4T_{2g}$ state and then to the ground $^4A_{2g}$ state via crossover points without emission of light (Figure S8 in the Supporting Information). The sample demonstrates decent luminescence thermal stability at the operational temperature of LED bulbs. A moderate red shift and broadening of the emission peak with the increasing temperature were also observed (Figure S9 in the Supplementary Information).

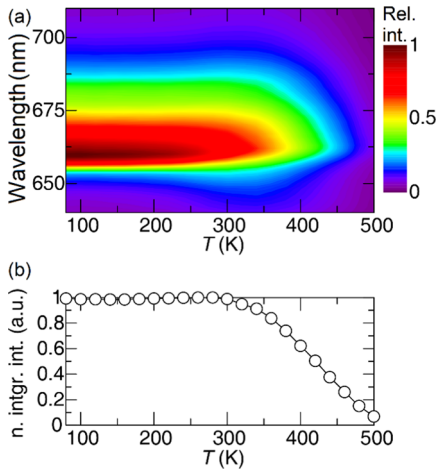

Figure 10. Contour plot of the temperature-dependent PL spectra for $K_2SrGe_{7.995}O_{18}$:0.005Mn^{4+} (a) and the normalized integrated intensity of its emission as a function of temperature (b).

The thermal quenching activation energy (ΔE) can be calculated from the following equation[67]

$$I_T = \frac{I_0}{1 + A\exp\left(\frac{-\Delta E}{kT}\right)}$$

where I_T is the emission intensity at a given temperature, I_0 is the emission intensity at room temperature, k is the Boltzmann constant, A is a constant for the host material, and ΔE is the activation energy. By plotting $\ln(I_0/I_T - 1)$ vs $1/kT$ from the experimental data and the following linear fitting (Figure S10), the activation energy ΔE was found to be 0.33 eV for the $K_2SrGe_{7.995}O_{18}$:0.005Mn^{4+} sample.

4. CONCLUSIONS

Single-crystal X-ray diffraction was used to study the structures of three new Na−Sr and K−Sr germanates, $Na_{0.36}Sr_{0.82}Ge_4O_9$ (**1**), $Na_2SrGe_6O_{14}$ (**2**), and $K_2SrGe_8O_{18}$ (**3**); **2** and **3** adopt known structural types with primitive unit cells and **1** demonstrates a rare example of the Ge polyhedra connection and has a rhombohedral lattice. The new phases doped with Pr^{3+} (**2**) and Mn^{4+} (**2** and **3**) exhibit the red emission upon UV excitation. The phosphorescence intensity of Mn^{4+}-doped $Na_2SrGe_6O_{14}$ (**2**) and $K_2SrGe_8O_{18}$ (**3**) was optimized by adjusting the doping level. The temperature-dependent phosphorescence spectra of $K_2SrGe_{7.995}O_{18}$:0.005Mn^{4+} showed that the material loses half of the low-temperature intensity at 420 K, which is above the normal LED lamps' operating temperature range. Further research should focus on the application of the $K_2SrGe_8O_{18}$ (**3**) phase rather than the $Na_2SrGe_6O_{14}$ (**2**) compound. Furthermore, the $Na_2SrGe_6O_{14}$ (**2**) phase also exhibits nonlinear optical properties, yet the SHG activity of the phase is low.

■ ASSOCIATED CONTENT

Supporting Information

The Supporting Information is available free of charge at https://pubs.acs.org/doi/10.1021/acs.inorgchem.2c01364.

Rietveld refinement of the $Na_2SrGe_{5.992}O_{14}$:0.008Mn^{4+}sample; Rietveld refinement of the $K_2SrGe_{7.995}O_{18}$:0.005Mn^{4+} sample; differential thermal analysis (DTA) curve (heating) for the $SrGe_4O_9$

https://doi.org/10.1021/acs.inorgchem.2c01364
Inorg. Chem. 2022, 61, 9364−9374

phase; experimental data and the Le Bail simulation ($R3_2$ and C_2 space groups) for $Na_{0.36}Sr_{0.82}Ge_4O_9$; fragment of Figure S1 at 50−80° 2θ range; temperature-dependent emission spectra of the $Na_2SrGe_{5.992}O_{14}$:0.008Mn^{4+} sample in the 100−500 K range; temperature-dependent emission spectra of the $K_2SrGe_{7.995}O_{18}$:0.005Mn^{4+} sample in two temperature regions; schematic configurational coordinate diagram for Mn^{4+}; normalized temperature-dependent emission spectra of the $K_2SrGe_{7.995}O_{18}$:0.005Mn^{4+} sample in the 77−520 K range; and linear fitting of the $\ln(I_0/IT-1)$ vs $1/kT$ data for the $K_2SrGe_{7.995}O_{18}$:0.005Mn^{4+} sample (PDF)

Accession Codes

CCDC 2166419−2166421 contain the supplementary crystallographic data for this paper. These data can be obtained free of charge via www.ccdc.cam.ac.uk/data_request/cif, or by emailing data_request@ccdc.cam.ac.uk, or by contacting The Cambridge Crystallographic Data Centre, 12 Union Road, Cambridge CB2 1EZ, UK; fax: +44 1223 336033.

■ AUTHOR INFORMATION

Corresponding Author

Yurij Mozharivskyj − *Department of Chemistry and Chemical Biology, McMaster University, Hamilton, Ontario L8S 4M1, Canada;* orcid.org/0000-0003-4498-5545; Email: mozhar@mcmaster.ca

Authors

Sergei A. Novikov − *Department of Chemistry and Chemical Biology, McMaster University, Hamilton, Ontario L8S 4M1, Canada*

Yimin Lu − *Department of Chemistry and Chemical Biology, McMaster University, Hamilton, Ontario L8S 4M1, Canada*

Weiguo Zhang − *Department of Chemistry, University of Houston, Houston, Texas 77204, United States*

P. Shiv Halasyamani − *Department of Chemistry, University of Houston, Houston, Texas 77204, United States;* orcid.org/0000-0003-1787-1040

Shruti Hariyani − *Department of Chemistry, University of Houston, Houston, Texas 77204, United States*

Jakoah Brgoch − *Department of Chemistry, University of Houston, Houston, Texas 77204, United States;* orcid.org/0000-0002-1406-1352

Vladislav V. Klepov − *Department of Chemistry and Biochemistry, University of South Carolina, Columbia, South Carolina 29208, United States;* orcid.org/0000-0002-2039-2457

Hans-Conrad zur Loye − *Department of Chemistry and Biochemistry, University of South Carolina, Columbia, South Carolina 29208, United States;* orcid.org/0000-0001-7351-9098

Complete contact information is available at: https://pubs.acs.org/10.1021/acs.inorgchem.2c01364

Notes

The authors declare no competing financial interest.

■ ACKNOWLEDGMENTS

S.N., Y.L., and Y.M. were supported by the Discovery Grant from the Natural Sciences and Engineering Research Council of Canada. S.H. and J.B. would like to thank the National Science Foundation (CER-1911311) as well as the Welch Foundation (E-1981) for funding this work. This work was also supported by the Texas Center for Superconductivity at the University of Houston (TcSUH). V.K. and H.-C.z.L., University of South Carolina, acknowledge NSF support via award DMR-1806279. P.S.H. and W.Z. thank the National Science Foundation (DMR-2002319) and Welch Foundation (Grant E-1457) for support.

■ REFERENCES

(1) Carone, D.; Usman, M.; Klepov, V. V.; Smith, M. D.; Kocevski, V.; Besmann, T. M.; zur Loye, H.-C. New germanate and mixed cobalt germanate salt inclusion materials: $[(Rb_6F)(Rb_4F)][Ge_{14}O_{32}]$ and $[(Rb_6F)(Rb_{3.1}Co_{0.9}F_{0.96})][Co_{3.8}Ge_{10.2}O_{30}F_2]$. *CrystEngComm* **2020**, *22*, 8072−8080.

(2) Usman, M.; Kocevski, V.; Smith, M. D.; Morrison, G.; Zhang, W.; Besmann, T.; Halasyamani, P. Shiv.; zur Loye, H.-C. Polymorphism and Molten Nitrate Salt-Assisted Single Crystal to Single Crystal Ion Exchange in the Cesium Ferrogermanate Zeotype: $CsFeGeO_4$. *Inorg. Chem.* **2020**, *59*, 9699−9709.

(3) Usman, M.; Smith, M. D.; Kocevski, V.; Besmann, T.; zur Loye, H.-C. Complex cobalt silicates and germanates crystallizing in a porous three-dimensional framework structure. *CrystEngComm* **2020**, *22*, 1112−1119.

(4) Carone, D.; Morrison, G.; Smith, M. D.; zur Loye, H.-C. Crystal Growth of New Germanate Framework Structures: Impact of the Presence of Square Planar Copper Species and Mixed Ge/Mn Sites on the Overall Structures of $Rb_2Cu_3Ge_5O_{14}$, $Cs_2Cu_3Ge_5O_{14}$, $Cs_7Cu_2Ge_{11}O_{27}F$, and $[(Cs_6F)(Cs_3AgF)][Ge_{12}Mn_2O_{32}]$. *Cryst. Growth Des.* **2022**, *22*, 3319−3325.

(5) F., Liebau, *Structural Chemistry of Silicates: Structure, Bonding, and Classification*; Springer Science & Business Media, 2012.

(6) Liang, S.; Shang, M.; Lian, H.; Li, K.; Zhang, Y.; Lin, J. Deep red MGe_4O_9:Mn^{4+} (M = Sr, Ba) phosphors: structure, luminescence properties and application in warm white light emitting diodes. *J. Mater. Chem. C* **2016**, *4*, 6409−6416.

(7) Kunitomo, J.; Suzuki, R.; Takahashi, Y.; Miyazaki, T.; Terakado, N.; Fujiwara, T. Red-emissive Mn-doped $Li_2Ge_4O_9$ phase synthesized via glass-ceramic route. *J. Ceram. Soc. Jpn.* **2014**, *122*, 725−727.

(8) Omel'chenko, K. S.; Khmelenko, O. V.; Panchenko, T. V.; Volnyanskii, M. D. Photoluminescence of manganese-doped $LiNaGe_4O_9$ crystals. *Phys. Solid State* **2014**, *56*, 751−756.

(9) Li, P.; Brik, M. G.; Li, L.; Han, J.; Li, X.; Peng, M. Prediction on Mn^{4+}-Doped Germanate Red Phosphor by Crystal Field Calculation on Basis of Exchange Charge Model: A Case Study on $K_2Ge_4O_9$:Mn^{4+}. *J. Am. Ceram. Soc.* **2016**, *99*, 2388−2394.

(10) Singh, S. P.; Kim, M.; Park, W. B.; Lee, J.-W.; Sohn, K.-S. Discovery of a Red-Emitting $Li_3RbGe_8O_{18}$:Mn^{4+} Phosphor in the Alkali-Germanate System: Structural Determination and Electronic Calculations. *Inorg. Chem.* **2016**, *55*, 10310−10319.

(11) Xue, J.; Ran, W.; Noh, H. M.; Choi, B. C.; Park, S. H.; Jeong, J. H.; Kim, J. H. Influence of alkaline ions on the luminescent properties of Mn^{4+}-doped MGe_4O_9 (M = Li_2, LiNa and K_2) red-emitting phosphors. *J. Lumin.* **2017**, *192*, 1072−1083.

(12) Ding, X.; Zhu, G.; Geng, W.; Wang, Q.; Wang, Y. Rare-Earth-Free High-Efficiency Narrow-Band Red-Emitting Mg3Ga2-GeO8:Mn4+ Phosphor Excited by Near-UV Light for White-Light-Emitting Diodes. *Inorg. Chem.* **2016**, *55*, 154−162.

(13) Ding, X.; Wang, Q.; Wang, Y. Rare-earth-free red-emitting $K_2Ge_4O_9$:Mn^{4+} phosphor excited by blue light for warm white LEDs. *Phys. Chem. Chem. Phys.* **2016**, *18*, 8088−8097.

(14) Takahashi, Y.; Fujiwara, T.; Benino, Y.; Komatsu, T. Crystallization and Raman Spectra of Langasite-Type $Na_2CaGe_6O_{14}$, $Na_2SrGe_6O_{14}$ and $Pb_3Ga_2Ge_4O_{14}$ in Corresponding Glasses. *Key Eng. Mater.* **2010**, *421−422*, 213−216.

(15) Takeda, H.; Uecker, R.; Kumatoriya, M.; Shimamura, K.; Reiche, P.; Fukuda, T. Growth and Characterization of $Na_2CaGe_6O_{14}$ Single Crystals. *Cryst. Res. Technol.* **1997**, *32*, 939−945.

(16) Shannon, R. D. Revised effective ionic radii and systematic studies of interatomic distances in halides and chalcogenides. *Acta Crystallogr., Sect. A* **1976**, *32*, 751−767.
(17) Thorington, L. Temperature Dependence of the Emission of an Improved Manganese-Activated Magnesium Germanate Phosphor. *J. Opt. Soc. Am.* **1950**, *40*, 579−583.
(18) Pust, P.; Schmidt, P. J.; Schnick, W. A revolution in lighting. *Nat. Mater.* **2015**, *14*, 454−458.
(19) Xia, Z.; Liu, Q. Progress in discovery and structural design of color conversion phosphors for LEDs. *Prog. Mater. Sci.* **2016**, *84*, 59−117.
(20) Nair, G. B.; Swart, H. C.; Dhoble, S. J. A review on the advancements in phosphor-converted light emitting diodes (pc-LEDs): Phosphor synthesis, device fabrication and characterization. *Prog. Mater. Sci.* **2020**, *109*, No. 100622.
(21) Amarasinghe, D. K.; Rabuffetti, F. A. Bandshift Luminescence Thermometry Using Mn^{4+}:$Na_4Mg(WO_4)_3$ Phosphors. *Chem. Mater.* **2019**, *31*, 10197−10204.
(22) Cai, P.; Wang, X.; Seo, H. J. Excitation power dependent optical temperature behaviors in Mn^{4+} doped oxyfluoride $Na_2WO_2F_4$. *Phys. Chem. Chem. Phys.* **2018**, *20*, 2028−2035.
(23) Glais, E.; Đorđević, V.; Papan, J.; Viana, B.; Dramićanin, M. D. $MgTiO_3$:Mn^{4+} a multi-reading temperature nanoprobe. *RSC Adv.* **2018**, *8*, 18341−18346.
(24) Tang, X.; Li, X.; Zou, Z.; Ma, Z.; Zhang, J.; Wang, Z.; Ci, Z.; Wang, D.; Peng, S.; Li, H.; Wang, Y. A thermal-sensitizing and thermochromic phosphor. *J. Mater. Chem. C* **2017**, *5*, 10369−10374.
(25) Dunaeva, E. E.; Ivleva, L. I.; Doroshenko, M. E.; Boldyrev, K. N.; Papashvili, A. G. Growth and spectral-luminescence characteristics of modified BGO crystals. *J. Cryst. Growth* **2019**, *525*, No. 125205.
(26) Lipina, O. A.; Melkozerova, M. A.; Chufarov, A. Yu.; Baklanova, Y. V.; Surat, L. L.; Tyutyunnik, A. P.; Zubkov, V. G. Structure−luminescence relationship in Eu^{3+}-doped $Sr_3La_2(Ge_3O_9)_2$ phosphors. *Opt. Mater.* **2019**, *87*, 145−150.
(27) Huang, Q.; Ye, W.; Hu, G.; Liu, X. Strong red emission in Bi^{3+} and Mn^{4+} codoped $Mg_{3.5}Ge_{1.25}O_6$ phosphors applied in optical agriculture. *J. Lumin.* **2019**, *210*, 89−95.
(28) Jung, I. H.; Auh, K. H. Crystal growth and piezoelectric properties of langasite ($La_3Ga_5SiO_{14}$) crystals. *Mater. Lett.* **1999**, *41*, 241−246.
(29) Hellenbrandt, M. The Inorganic Crystal Structure Database (ICSD)—Present and Future. *Crystallogr. Rev.* **2004**, *10*, 17−22.
(30) Smolin, Y. I. *Crystal Structure of Barium Tetragermanate*; Doklady Akademii Nauk SSSR, 1968; Vol. *181*, pp 595−598.
(31) Nishi, F. Strontium Tetragermanate, $SrGe_4O_9$. *Acta Crystallogr., Sect. C: Cryst. Struct. Commun.* **1996**, *52*, 2393−2395.
(32) Fleet, M. E.; Muthupari, S. Structure of $A_2Ge_4O_9$-Type Sodium Tetragermanate ($Na_2Ge_4O_9$) and Comparison with Other Alkali Germanate and Silicate Mixed Tetrahedral−Octahedral Framework Structures. *J. Solid State Chem.* **1998**, *140*, 175−181.
(33) Redhammer, G. J.; Tippelt, G. The tetragermanates $A_2Ge_4O_9$ (A = Na, K and Rb). *Acta Crystallogr., Sect. C: Cryst. Struct. Commun.* **2013**, *69*, 995−1001.
(34) Redhammer, G. J.; Tippelt, G. The polar phase of $Li_2Ge_4O_9$ at 298, 150 and 90 K. *Acta Crystallogr., Sect. C: Cryst. Struct. Commun.* **2013**, *69*, 1091−1095.
(35) Baumgartner, O.; Völlenkle, H. Die Kristallstruktur des Tetragermanats $K_2Ba[Ge_4O_9]_2$. *Monatsh. Chem.* **1978**, *109*, 1145−1153.
(36) *Stoe & Cie, X-AREA, X-RED32 and X-SHAPE*, (version 1.31), (version 1.31), (version 2.05); Stoe & Cie: Darmstadt, Germany, 2005.
(37) Sheldrick, G. M. SHELXT − Integrated space-group and crystal-structure determination. *Acta Crystallogr., Sect. A: Found. Adv.* **2015**, *71*, 3−8.
(38) Sheldrick, G. M. Crystal structure refinement with SHELXL. *Acta Crystallogr., Sect. C: Cryst. Struct.* **2015**, *71*, 3−8.
(39) Dolomanov, O. V.; Bourhis, L. J.; Gildea, R. J.; Howard, J. A. K.; Puschmann, H. Puschmann, OLEX2: a complete structure solution, refinement and analysis program. *J. Appl. Crystallogr.* **2009**, *42*, 339−341.
(40) Hunter, B. In Rietica - a Visual Rietveld Program, International Union of Crystallography Commission on Powder Diffraction Newsletter *Rietica - A Visual Rietveld Program*, 1998.
(41) Kubelka, P.; Munk, F. Ein Beitrag Zur Optik Der Farbanstriche. *Z. Tech. Phys.* **1931**, *12*, 593−601.
(42) *Modern Aspects of Reflectance Spectroscopy*, Wendlandt, W. W., Ed.; Springer: US, 1968.
(43) Kresse, G.; Furthmüller, J. Efficiency of ab-initio total energy calculations for metals and semiconductors using a plane-wave basis set. *Comput. Mater. Sci.* **1996**, *6*, 15−50.
(44) Kresse, G.; Furthmüller, J. Efficient iterative schemes for ab initio total-energy calculations using a plane-wave basis set. *Phys. Rev. B* **1996**, *54*, 11169−11186.
(45) Perdew, J. P.; Burke, K.; Ernzerhof, M. Generalized Gradient Approximation Made Simple. *Phys. Rev. Lett.* **1996**, *77*, 3865−3868.
(46) Blöchl, P. E. Projector augmented-wave method. *Phys. Rev. B* **1994**, *50*, 17953−17979.
(47) Kresse, G.; Joubert, D. From ultrasoft pseudopotentials to the projector augmented-wave method. *Phys. Rev. B* **1999**, *59*, 1758−1775.
(48) Gagné, O. C.; Hawthorne, F. C. Bond-length distributions for ions bonded to oxygen: metalloids and post-transition metals. *Acta Crystallogr., Sect. C: Cryst. Struct.* **2018**, *74*, 63−78.
(49) Blatov, V. A.; Shevchenko, A. P.; Proserpio, D. M. Applied Topological Analysis of Crystal Structures with the Program Package ToposPro. *Cryst. Growth Des.* **2014**, *14*, 3576−3586.
(50) Zachariasen, W. H. The crystal structure of benitoite $BaTiSi_3O_9$. *Z. Kristallogr. - Cryst. Mater.* **1930**, *74*, 139−146.
(51) Bush, A. A.; Stefanovich, S..Y. Piezoelectric and Nonlinear Optical Properties of PbGe4O9 Crystals. *Inorg. Mater.* **2002**, *38*, 168−171.
(52) APEX4 Software, (n.d.). https://www.bruker.com/en/products-and-solutions/diffractometers-and-scattering-systems/single-crystal-x-ray-diffractometers/sc-xrd-software/apex.html (accessed October 22, 2021).
(53) Kaminskii, A. A.; Mill, B. V.; Khodzhabagyan, G. G.; Konstantinova, A. F.; Okorochkov, A. I.; Silvestrova, I. M. Investigation of trigonal $(La_{1-x}Nd_x)_3Ga_5SiO_{14}$ crystals. I. Growth and optical Properties. *Phys. Status Solidi (a)* **1983**, *80*, 387−398.
(54) Novikov, S. A.; Mozharivskyj, Y. Synthesis and structure of the Na−Ba and Rb−Ba octagermanates and phosphorescence of the $Rb_2BaGe_{8-x}O_{18}$:xMn^{4+} series. *J. Solid State Chem.* **2021**, *304*, No. 122607.
(55) G., Blasse; B. C., Grabmaier*Luminescent Materials*; Springer-Verlag: Berlin Heidelberg, 1994.
(56) Lü, W.; Lv, W.; Zhao, Q.; Jiao, M.; Shao, B.; You, H. A Novel Efficient Mn^{4+} Activated $Ca_{14}Al_{10}Zn_6O_{35}$ Phosphor: Application in Red-Emitting and White LEDs. *Inorg. Chem.* **2014**, *53*, 11985−11990.
(57) Lin, H.; Hu, T.; Huang, Q.; Cheng, Y.; Wang, B.; Xu, J.; Wang, J.; Wang, Y. Non-Rare-Earth K_2XF_7:Mn^{4+} (X = Ta, Nb): A Highly-Efficient Narrow-Band Red Phosphor Enabling the Application in Wide-Color-Gamut LCD. *Laser Photonics Rev.* **2017**, *11*, No. 1700148.
(58) Wang, B.; Lin, H.; Huang, F.; Xu, J.; Chen, H.; Lin, Z.; Wang, Y. Non-Rare-Earth $BaMgAl_{10-2x}O17$:xMn^{4+},xMg^{2+}: A Narrow-Band Red Phosphor for Use as a High-Power Warm w-LED. *Chem. Mater.* **2016**, *28*, 3515−3524.
(59) Li, X.; Chen, Z.; Wang, B.; Liang, R.; Li, Y.; Kang, L.; Liu, P. Effects of Impurity Doping on the Luminescence Performance of Mn^{4+}-Doped Aluminates with the Magnetoplumbite-Type Structure for Plant Cultivation. *Materials* **2018**, *12*, No. 86.
(60) Peng, M.; Yin, X.; Tanner, P. A.; Brik, M. G.; Li, P. Site Occupancy Preference, Enhancement Mechanism, and Thermal Resistance of Mn^{4+} Red Luminescence in $Sr_4Al_{14}O_{25}$: Mn^{4+} for Warm WLEDs. *Chem. Mater.* **2015**, *27*, 2938−2945.

(61) Brik, M. G.; Camardello, S. J.; Srivastava, A. M. Influence of Covalency on the Mn^{4+} $^2E_g \rightarrow {}^4A_{2g}$ Emission Energy in Crystals. *ECS J. Solid State Sci. Technol.* **2015**, *4*, R39−R43.
(62) Shao, Q.; Lin, H.; Hu, J.; Dong, Y.; Jiang, J. Temperature-dependent photoluminescence properties of deep-red emitting Mn^{4+}-activated magnesium fluorogermanate phosphors. *J. Alloys Compd.* **2013**, *552*, 370−375.
(63) B., Henderson; G. F., Imbusch *Optical Spectroscopy of Inorganic Solids*;Oxford University Press: Oxford, New York, 2006.
(64) R. C., Powell *Physics of Solid-State Laser Materials*; Springer-Verlag: New York, 1998. https://www.springer.com/gp/book/9781563966583 (accessed December 14, 2020).
(65) Uylings, P. H. M.; Raassen, A. J. J.; Wyart, J. F. Energies of N equivalent electrons expressed in terms of two-electron energies and independent three-electron parameters: a new complete set of orthogonal operators. II. Application to 3dN configurations. *J. Phys. B: At. Mol. Phys.* **1984**, *17*, 4103−4126.
(66) Baur, F.; Jüstel, T. Dependence of the optical properties of Mn^{4+} activated $A_2Ge_4O_9$ (A = K,Rb) on temperature and chemical environment. *J. Lumin.* **2016**, *177*, 354−360.
(67) Bhushan, S.; Chukichev, M. V. Temperature dependent studies of cathodoluminescence of green band of ZnO crystals. *J. Mater. Sci. Lett.* **1988**, *7*, 319−321.

https://doi.org/10.1021/acs.inorgchem.2c01364
Inorg. Chem. 2022, 61, 9364−9374